Energy Advances

ROYAL SOCIETY OF CHEMISTRY

PAPER

View Article Online
View Journal | View Issue

Cite this: *Energy Adv.*, 2022, 1, 562

Bimetallic iron cobalt oxide nanoclusters embedded on three-dimensional flower-like iron cobalt oxide nanosheets for improved oxygen evolution reaction†

Ayyavu Shankar and Govindhan Maduraiveeran *

The design of the nanoarchitecture of hierarchical three-dimensional (3D) nanosheets for use as free-standing, non-precious electrocatalysts for oxygen evolution reaction (OER) is critical for building commercial water-splitting systems. Herein, we report a facile, scalable, efficient and binder-free fabrication of earth-abundant bimetallic iron cobalt oxide nanoclusters embedded on 3D flower-like iron cobalt oxide nanosheets (FeCoO NC@3D-FeCoO NS) grown on a nickel foam (NF) substrate for the improved OER under an alkaline electrolyte. The as-developed FeCoO NC@3D-FeCoO NS|NF electrode materials exhibited an excellent OER catalytic activity with low OER onset potential (~1.37 V), small overpotential (η) (~0.22 V) @ 10 mA cm^{-2} and Tafel slope (~53 mV dec^{-1}), high mass activity (500 A g^{-1}) and turn over frequency (TOF) (2.83 s^{-1}), and long-term durability (over 100 h) in 1.0 M KOH. The attained high catalytic OER performance of the FeCoO NC@3D-FeCoO NS|NF electrode is due to its unique bimetallic heterostructure, rich in oxygen deficient sites and active sites, large electrochemical active surface area (ECASA), low polarization resistance, rapid charge-transfer kinetics, facilitation of mass diffusion/transport of OH^- ions and improved electronic conductivity, and ease of H_2O adsorption onto nearby active sites. Impressively, the FeCoO NC@3D-FeCoO NS|NF‖PtC/C couple exhibited less positive potential (~1.82 V) to attain a current density of ~50 mA cm^{-2} and high catalytic OER performance, which is ~150.0 mV smaller than that of the benchmark RuO_2‖Pt/C couple in the alkaline electrolysis cell, suggesting good practicability.

Received 27th April 2022,
Accepted 11th July 2022

DOI: 10.1039/d2ya00095d

rsc.li/energy-advances

Introduction

Electrocatalytic water splitting is one of the most encouraging methods for resolving the energy issue since it can convert "waste power" (solar and wind) into renewable energy sources like green hydrogen (H_2) energy.[1–3] Unavoidably, the sluggish anodic oxygen evolution reaction (OER) significantly impedes the complete process of water splitting because of its multistep proton-coupled four-electron transfer processes.[4–7] Iridium and ruthenium based metal and metal oxides are currently considered as the state-of-the-art catalysts, but their high cost and scarcity severely limit their commercial application for large-scale use.[8–11] As a result, a lot of research studies have focused on the design of low-cost OER electrocatalysts based on first-row transition metals and their oxides including cobalt oxide nanoparticles, iron oxide, nickel oxide, manganese oxide composite thin films, *etc.*[12–18]

Over the past few decades, transition metal oxide (TMO)-based nanomaterials have offered a range of possible unique features such as shape- and size-dependent properties, high crystallinity, high surface energy and other chemical composition related characteristics that can contribute to electrocatalytic properties.[19–23] Nonetheless, because of their undesirable adsorption energy (ΔE) of the chemical intermediates and weak conductivity, the apparent performance of virgin metal oxides is often unsatisfactory.[24] Particularly, the non-precious transition metal-based spinel oxide compounds (SOCs) such as Co_3O_4, $NiFe_2O_4$, $NiCo_2O_4$, $CoMn_2O_4$, $CoFe_2O_4$, *etc.* have been investigated for OER performance.[16,25–29] The partial substitution of an active redox element Fe (d^6) may result in increased d-electron deficiency, favouring OER features. To date, numerous approaches on non-noble metal-based SOCs have been used to compete with the high OER performance of noble metal-based catalysts, including regulating phase composition, shape, and intrinsic defects and metal doping.[30–33] For example, Basu *et al.*[34] developed a 2D structure for cobalt iron oxide ($CoFe_2O_4$) that was

Materials Electrochemistry Laboratory, Department of Chemistry, SRM Institute of Science and Technology, Kattankulathur, Tamil Nadu-603 203, India.
E-mail: maduraig@srmist.edu.in

† Electronic supplementary information (ESI) available. See DOI: https://doi.org/10.1039/d2ya00095d

used in OER. The as-synthesised $CoFe_2O_4$ only needed a ~410 mV overpotential to reach a current density of 10 mA cm^{-2} in 1.0 M KOH. Li *et al.*[31] constructed a sequence of MFe_2O_4 (M = Co, Ni, Cu, and Mn) nanofibers, and discovered that $CoFe_2O_4$ with spinel structures exhibited good catalytic activity towards OER with an overpotential of ~0.40 V @ 5 mA cm^{-2}. More recently, Zhang *et al.*[35] reported a highly effective electrocatalyst for OER consisting of bimetallic cobalt iron oxide ($CoFe_2O_4$) with a nanosphere structure which required an overpotential of ~0.28 V to reach a current density of 10 mA cm^{-2} under an alkaline electrolyte. Research studies demonstrated that direct fabrication of the spinel transition metal-based nanomaterials using an electrochemical method offers a wide range of advantages.[36–38] In the electrochemical method, the surface structure and composition of TMO nanomaterials may be easily controlled or altered by varying the current density/potential, deposition time, and choice and composition of precursors/additives.[39–42]

In this study, we demonstrate earth-abundant bimetallic iron cobalt oxide nanoclusters embedded on 3D flower-like iron cobalt oxide nanosheets (FeCoO NC@3D-FeCoO NS) directly grown on a nickel foam substrate through a one-step electrochemical strategy for the first time towards enhanced OER activity under an alkaline electrolyte. The present electrochemical fabrication of FeCoO NC embedded on 3D-FeCoO NS nanomaterials offered the following merits: (i) easy single-step fabrication approach; (ii) hard or soft template- and binder-free strategy; (iii) low cost and short time approach; (iv) ability to develop under mild experimental conditions and bulk scale production; (v) online continuous monitoring of the deposition process, which is useful for industrial scale operations; (vi) low power consumption by avoiding the calcination step and organic solvents; and (vii) exclusive surface morphology of FeCoO nanoclusters @ 3D flower-like iron cobalt oxide nanosheets, creating the potential interfacial reaction, effective chemical/interfacial distributions at the nanoscale, fast electron–electron transfer kinetics and high degree of solidity without using a binder. Owing to the unique bimetallic heterostructures, rich in oxygen deficient sites and active sites, high ECASA, low polarization resistance, and rapid charge-transfer kinetics, the as-fabricated FeCoO NC@3D-FeCoO NS electrode materials exhibited an outstanding catalytic OER activity with low OER onset potential, small overpotential (η) and Tafel slope, high mass activity, long-term durability, and low cell-voltage and high current density in the real alkaline water electrolyzer.

Experimental section

Chemical reagents

Ferric chloride anhydrous ($FeCl_3$), cobalt(II) nitrate hexahydrate ($Co(NO_3)_2{\cdot}6H_2O$), and potassium hydroxide pellets were purchased from Sigma Aldrich. Nitric acid was purchased from Alfa-Aesar. The commercial ruthenium(IV) oxide (RuO_2) and platinum carbon (PtC, 10%) were obtained from Sigma-Aldrich. All analytical grade reagents were used exactly as they were obtained. All the solutions in this investigation were made with pure water (18.2 M cm) collected from a NANO pure Diamond UV ultrapure water purification system.

Fabrication of the FeCoO NC@3D-FeCoO NS|NF Electrode

Typically, a single-step electrochemical deposition approach was adopted to fabricate FeCoO NC@3D-FeCoO NS nanostructures on a cleaned NF electrode substrate with a geometric surface area of ~0.12 cm^2. The NF electrodes were well-cleaned by sequential sonication for 15 min in water, acetone, and isopropanol prior to the electrodeposition process. Continuous cyclic voltammetry (CV) measurements were applied for the pre-cleaned NF electrode in the electrolyte solution consisting of 0.05 M cobalt(II) nitrate ($Co(NO_3)_2{\cdot}6H_2O$) and 0.05 M iron(III) chloride ($FeCl_3$) + 0.1 M HNO_3 solution for five continuous cycles at a scan rate of 5.0 mV s^{-1}. The operating potential window was chosen between of ~−0.16 and ~1.63 V *vs.* reverse hydrogen electrode (RHE). The as-fabricated electrode was washed numerous times with DI water and 100% ethanol after the electrodeposition, and was designated as FeCoO NC@3D-FeCoO NS|NF. The mass loading of the catalyst of FeCoO NC@3D-FeCoO nanosheets was measured to be ~0.16 cm^{-2}. In order to compare the OER activity, the single iron and cobalt oxides were made using the same procedure as described above. The commercially available state-of-the-art RuO_2 and Pt/C catalyst ink was made by dispersing ~5.0 mg of catalyst in 0.5 mL of DI water containing 1.0% Nafion. The catalyst ink was ultrasonically dispersed for around 30 minutes, resulting in a highly dispersed catalyst ink. The catalyst ink (~10 μL) was drop cast onto an NF (RuO_2|NF and Pt-C|NF) surface and dried at room temperature.

Characterisation of the FeCoO NC@3D-FeCoO NS|NF electrode

High-resolution scanning electron microscopy (HR-SEM, FEI QUANTA 200 with a 20 kV accelerating voltage) and transmission electron microscopy (TEM, JEOL 2010F) with energy-dispersive X-ray spectroscopy (EDX) were used for the morphological and elemental analyses of the FeCoO NC@3D-FeCoO NS|NF electrode. An X-ray diffractometer (XRD, PANanalytical-Xpert Pro diffractometer with a Ni filtered monochromatic Cu Kr (1.5406, 2.2 KW Max)) was used to examine the crystalline structures of FeCoO NC@3D-FeCoO NS|NF. X-ray photoelectron spectroscopy (XPS, PHI Versaprobe III) was employed to study the change in the binding energies of Co, Fe, and O elements and the composition of the developed nanomaterials. The water contact angles were measured using a surface/interface tension goniometer (DMs-401) by dropping 2 μL of DI water on samples at room temperature. All electrochemical tests were performed with the three standard electrode cell setup using Biologic workstation (VSP-300) in a 1.0 M KOH electrolyte. Nickel foam (NF; geometrical surface area: ~0.12 cm^{-2}) was used as the working electrode, Pt coil was employed as the counter electrode and Ag/AgCl (3.0 M KCl) acted as the reference electrode. Electrochemical impedance spectroscopy (EIS) was carried out with the frequency range of 100 kHz to 50 mHz.

All the electrodes' potential against the Ag/AgCl ($E_{Ag|AgCl}$) electrode was converted to potential *vs.* RHE (E_{RHE}) by eqn (1):[36]

$$E_{RHE} = E_{Ag|AgCl} + E^{\circ}_{RHE} = E_{Ag|AgCl} + 1.036 \quad (1)$$

On the other hand, the overpotential for OER can be obtained with the help of eqn (2):

$$\eta_j = (E_{Ag|AgCl} + 1.036) - 1.23 \quad (2)$$

where subscript j represents the current density at a given potential.

The mass activity (A g^{-1}) value of the electrodes was calculated from the electrocatalyst loading m (0.02 mg cm^{-2}) and the observed current density j (mA cm^{-2}) at an overpotential of ~220 mV:

$$\text{Mass activity} = \frac{j}{m} \quad (3)$$

The electrochemical active surface area (ECSA) of the FeCoO NC@3D-FeCoO NS|NF electrode was computed using double-layer capacitance (C_{dl}, mF) and specific capacitance (C_S, mF cm^{-2}), which were measured using cyclic voltammetry (CV) at various scan rates:

$$\text{ECSA} = C_{dl}/C_S \quad (4)$$

The TOF of the electrocatalysts was determined by eqn (5):[43,44]

$$\text{TOF} = \frac{jS}{4F_n} \quad (5)$$

where "j" is the current density in mA cm^{-2} at the overpotential of ~220 mV, "S" is the geometrical surface area of the electrode (~0.12 cm^{-2}), "F" is the Faraday constant (96 485 C mol^{-1}), and "n", the number of moles of active sites of the electrode, is given by the following equation:

$$n = \frac{m_{mass}}{M} \quad (6)$$

with m_{mass} the mass loading of active materials and M the molar mass of active materials.[45]

Results and discussion

Fig. 1(a) shows the XRD pattern of the bimetallic iron cobalt oxide nanoclusters embedded on the 3D flower-like iron cobalt oxide nanosheet electrode (FeCoO NC@3D-FeCoO NS|NF). As displayed in Fig. 1(a), FeCoO NC@3D-FeCoO NS|NF exhibited three XRD peaks at ~18.2°, ~35.3° and ~36.9°, corresponding to the crystalline planes (111), (220) and (311) with the spinel phase structure of Fe–Co oxides (PDF#22-1086).[38,46,47] The XRD pattern of the pure iron oxide (Fig. 1(b)) nanomaterials displayed a peak at ~30.2° which was ascribed to the characteristic peaks of Fe oxides (JCPDS 39-1346).[48] As depicted in Fig. 1(c), the bare cobalt oxide nanostructure demonstrated three XRD peaks at ~31.3°, ~36.4° and ~42.3°, corresponding to the cubic phase of (220), (111) and (200) Co_3O_4 (JCPDS 48-1719).[49,50] Fig. 2(a–c) depicts the SEM images of the FeCoO NC@3D-FeCoO NS|NF (a), 3D-FeO NS|NF (b), and 3D-CoO NS|NF (c) electrodes. The hierarchical 3D flower like FeCoO nanostructures consisted

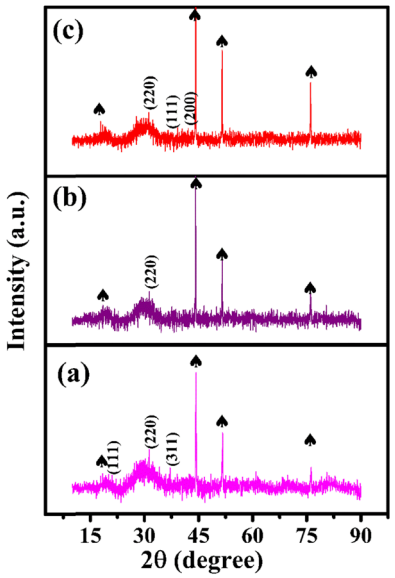

Fig. 1 XRD patterns of the FeCoO NC@3D-FeCoO NS|NF (a), 3D-FeO NS|NF (b), and 3D-CoO NS|NF (c) electrodes. The peaks marked with spades were derived from the NF substrate.

of 2D nanosheets. The diameter of the FeCoO nanosheets was found to be in the range of ~150–200 nm. As shown in Fig. 2(a), the average dimension of the 3D flower of FeCoO nanostructures was measured to be ~180 nm and the nanostructures were homogeneously dispersed. For comparison, pure 3D-FeO NS|NF and 3D-CoO NS|NF electrodes were fabricated under similar experimental conditions. The 3D-FeO NS|NF electrode (Fig. 2(b)) demonstrated similar 3D flower like surface morphology with an average dimension of ~211 nm. As can be easily seen in Fig. 2(c), the 3D-CoO NS|NF electrode showed the homogeneous dispersion of 3D-flower like surface structures with an average diameter of ~340 nm. Fig. 2(d) presents the elemental mapping of the FeCoO NC@3D-FeCoO NS|NF electrode. The elemental mapping results showed that Fe, Co and O elements were homogeneously dispersed on the electrode substrate. Based on the EDX data of Fig. S1 (ESI†), the elements of Fe and Co were existed in the FeCoO NC@3D-FeCoO NS|NF electrode.

Fig. 2(e) and (f) show the TEM and HRTEM images of the FeCoO NC@3D-FeCoO NS. As shown in Fig. 2(e, f) and Fig. S2a (ESI†), the FeCoO nanoclusters with an average dimension of ~2.8 nm were uniformly dispersed on 3D FeCoO nanosheets. The Fe and Co ions can primarily be adsorbed on to the rough surface of NiO. The resulting heterogeneous nucleation process may majorly take place on the direct growth of FeCo oxide clusters. Owing to its large surface-to-volume ratio, the 3D nanosheet-like structure offered abundant space to permit fast mass transport of ions through the electrolyte/electrode interface. The HRTEM image (Fig. 2(f)) of the FeCoO NC@3D-FeCoO NS showed an interplanar distance of ~0.29 nm, ascribed to the spinel plane of (220) FeCoO nanostructures. The selected area electron diffraction (SAED) pattern of the FeCoO NC@3D-FeCoO NS demonstrated well-defined diffraction spots with the crystalline planes of (331), (422), and (533). Furthermore, the

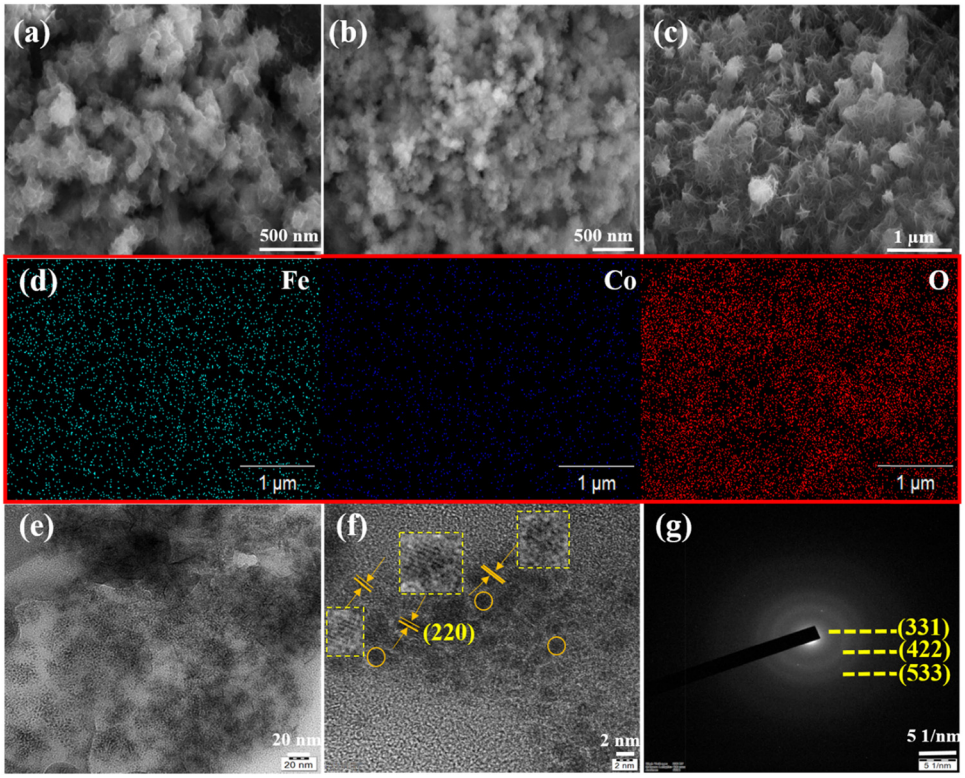

Fig. 2 SEM images of the FeCoO NC@3D-FeCoO NS|NF (a), 3D-FeO NS|NF (b), and 3D-CoO NS|NF (c) electrodes. The elemental mapping of the FeCoO NC@3D-FeCoO NS|NF electrode (d). TEM (e), HR-TEM (f), and SAED pattern (g) of the FeCoO NC@3D-FeCoO NS.

TEM-EDS measurements showed the co-existence of Fe, Co, and O elements (Fig. S2b, ESI†).

Fig. 3 displays the XPS spectra of the survey (a), and Fe 2p (b), Co 2p (c), and O 1s (d) regions of the FeCoO NC@3D-FeCoO NS|NF electrode. From the survey XPS spectra of Fig. 3(a), the presence of Fe, Co, and O elements was identified at the FeCoO NC@3D-FeCoO NS|NF electrode. The XPS results display an atomic ratio of Fe : Co : O of 2.8 : 1.0 : 35.6 for the FeCoO NC@3D-FeCoO NS|NF electrode. In Fig. 3(b), two peaks are observed for Fe $2p_{3/2}$ and Fe $2p_{1/2}$ located at ~709.3 and ~723.0 eV, and the Fe $2p_{3/2}$ and Fe $2p_{1/2}$ peaks are at ~711.3 and ~726.2 eV, revealing the presence of Fe^{2+} and Fe^{3+} in the FeCoO NC@3D-FeCoO NS|NF electrode.[51] In the Co 2p core level for the FeCoO NC@3D-FeCoO NS|NF electrode (Fig. 3(c)), the fitted Co 2p peak at ~781.3 eV can be attributed to Co^{2+}, whereas the peaks obtained at ~784.7 and ~788.6 eV can be attributed to Co^{3+}.[51] Moreover, the XPS spectra of O 1s are presented in Fig. 3(d), where two primary distinctive peaks at ~531.9 and ~530.9 eV, ascribed to the substituted OH^- group and lattice oxygen, respectively, are observed.[52] The surface wettability of the catalyst is determined by measuring its contact angle, which has consequences for constructing the electrode–electrolyte interface in test systems for electrochemical assessments. The hydrophilicity of the system facilitates improved interaction of the electrolyte with the catalyst in water electrolysis. Improved electrode/electrolyte interactions, in addition to active centres, would boost the OER catalytic performance. The water contact angle of the FeCoO NC@3D-FeCoO NS|NF electrode is found to be ~99.8° only, which is desirable for water wetting (Fig. S3(b), ESI†). It is anticipated that it was caused by the rough surface of the FeCoO NC@3D-FeCoO nanosheets, revealing their improved wettability nature. However, the contact angle of the bare NF with water is measured to be ~125.3°, indicating that the bare NF is highly hydrophobic (Fig. S3(a), ESI†). The improved hydrophilic rough surface is beneficial to OER because it exposes more active sites, which speeds up the release of O_2 bubbles and the diffusion of electrolytes.[53,54]

Primarily, the electrochemical redox characteristics of the FeCoO NC@3D-FeCoO NS|NF electrode were studied under 1.0 M KOH and are shown in Fig. S4 (ESI†). The as-fabricated FeCoO NC@3D-FeCoO NS|NF electrode exhibited an anodic peak at ~1.3 V (*vs.* RHE) and a couple of cathodic peaks at ~1.2 V and 1.0 V, ascribed to the redox couple of Fe^{3+}/Fe^{4+} and Co^{2+}/Co^{3+}.[55,56] Fig. S5(a) (ESI†) presents the CVs of the FeCoO NC@3D-FeCoO NS|NF electrode at different scanning rates, starting from 10.0 to 125.0 mV s^{-1}. The linear plots showed peak currents for both oxidation and reduction against the square root of the scan rate, revealing the typical diffusion-controlled process (Fig. S5(b), ESI†). Fig. 4(a) displays the LSV curves of the 3D-FeO NS|NF (black curve), FeCoO NC@3D-FeCoO NS|NF (green curve), 3D-CoO NS|NF (blue curve) and commercial RuO_2 (dark red curve) electrodes recorded in 1.0 M KOH at a scan rate of 20.0 mV s^{-1}. The as-developed FeCoO NC@3D-FeCoO NS|NF electrode (green curve) exhibited the lowest

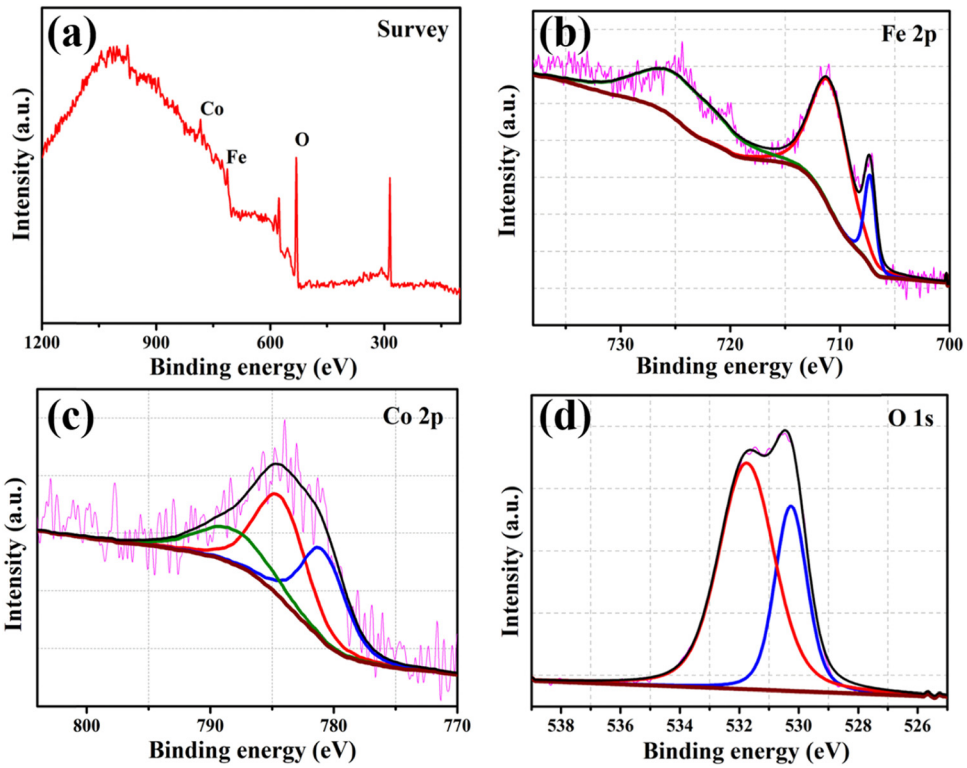

Fig. 3 XPS spectra of the FeCoO NC@3D-FeCoO NS|NF electrode: (a) survey and (b) Fe 2p, (c) Co 2p, and (d) O 1s regions.

OER onset potential (E_{onset}) of ~1.37 V and an overpotential (η_{10}) of ~0.22 V to attain a current density of 10 mA cm^{-2} in comparison to 3D-FeO NS|NF (E_{onset}: 1.47 V and η_{10}: 0.31 V), 3D-CoO NS|NF (E_{onset}: 1.51 V and η_{10}: 0.35 V) and commercial RuO_2 (E_{onset}: 1.46 V and η_{10}: 0.35 V) electrodes, as presented in Fig. 4(b) and 3(c). Fig. 4(d) depicts the Tafel plots of the various developed

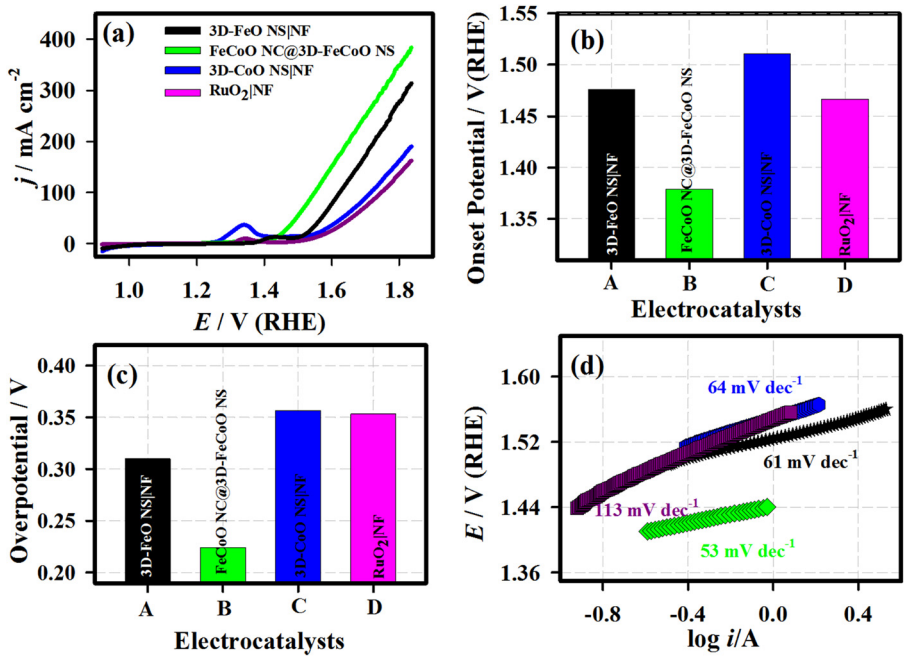

Fig. 4 LSV curves (a), OER onset potential (b) and measured overpotential @ 10 mA cm^{-2} (c), and Tafel plots (d) of the 3D-FeO NS|NF (black curve), FeCoO NC@3D-FeCoO NS|NF (green curve), 3D-CoO NS|NF (blue curve) and commercial RuO_2 (dark red curve) electrodes. Electrolyte: 1.0 M KOH; scan rate: 20.0 mV s^{-1}.

Table 1 Comparison of the electrochemical OER performance of the transition metal based electrocatalysts functioning in alkaline electrolytes

S. No.	Material	Synthetic method	Overpotential (η) (mV)	Current density (mA cm^{-2})	Tafel slope (mV dec^{-1})	Ref.
1	$FeCoO_x$-Vo-S	Thermal treatment	260	200	21.0	56
2	3D NiSe@$Ni_{1x}Fe_xSe_2$	Solvothermal	236	100	36.8	57
3	Co_3FeP_x	Thermal treatment	260	10	58.0	58
4	FeCo(Mn)–O/NF	Electrodeposition	235	10	44.5	59
5	$Ni_{1-x}Fe_x$ oxyhydroxide	Electrodeposition	300	50	30.0	60
6	$Ni_xCo_{3x}O_4$ NWs	Co-precipitation	269	10	120.0	61
7	CoFe LDH-S	Wet-chemistry process	270	10	58.3	62
8	CoFe LDH	Electrodeposition	250	10	35.0	63
9	FCND	Hydrothermal	300	50	77.0	64
10	Fe–Co–O/Co@NC/NF	Thermal decomposition	305	100	96.0	65
11	FeCoO NC@3D-FeCoO NS	Electrodeposition	218	10	53.0	This study

NF: nickel foam; NW: nanowire; NC: nanoclusters; NS: nanosheets; FCND: iron cobalt nickel dichalcogenides.

electrodes such as 3D-FeO NS|NF (black curve), FeCoO NC@3D-FeCoO NS|NF (green curve), 3D-CoO NS|NF (blue curve) and commercial RuO_2 (dark red curve) electrodes. The value of the Tafel slope was found to be ~61.0, ~53.0, ~64.0, and ~61.0 mV dec^{-1} for the 3D-FeO NS|NF, FeCoO NC@3D-FeCoO NS|NF, 3D-CoO NS|NF, and commercial RuO_2 electrodes, respectively. As displayed in Fig. 4(d), the FeCoO NC@3D-FeCoO NS|NF electrode demonstrated a small Tafel slope value of ~53 mV dec^{-1}, which is lower than that of other bimetallic oxides reported in the literature (Table 1).[57–66] The FeCoO NC@3D-FeCoO NS|NF electrode exhibited a high mass activity of 500.0 A g^{-1} at a low overpotential of ~0.22 V, which is more than ~1.5 and ~2.0 times that of the 3D-FeO NS|NF (333.3 A g^{-1}) and 3D-CoO NS|NF (250.0 A g^{-1}) electrodes. The turnover frequency (TOF) was also calculated to be 2.83 s^{-1} for the FeCoO NC@3D-FeCoO NS|NF electrode, which is ~13.0 and ~7.2 times higher than that of the 3D-FeO NS|NF (0.21 s^{-1}) and 3D-CoO NS|NF (0.39 s^{-1}) electrodes.

Fig. 5 shows the chronoamperometric (j *vs.* t) curves of the 3D-FeO NS|NF (black curve), FeCoO NC@3D-FeCoO NS|NF (green curve), 3D-CoO NS|NF (blue curve) and commercial RuO_2 (dark red curve) electrodes recorded at different applied potentials of ~1.59 V (a), ~1.65 V (b), and ~1.69 V (c) under 1.0 M KOH. As depicted in Fig. 5(d), the FeCoO NC@3D-FeCoO NS|NF electrode exhibited maximum OER current densities of ~114, ~160, and ~196 mA cm^{-2} at the applied potentials of 1.59, 1.65, and 1.69 V, respectively. The FeCoO NC@3D-FeCoO NS|NF electrode showed the best anodic current density at the applied potential of ~1.59, ~1.65, and ~1.69 V, which was over ~2.2, ~1.7 and ~1.5 and ~2.8, ~1.9, and ~1.6 times that of the 3D-FeO NS|NF and 3D-CoO NS|NF electrodes. The chronopotentiometric (E *vs.* t) measurements of Fig. 6 show that the FeCoO NC@3D-FeCoO NS|NF electrode possessed a less positive electrode potential at all the applied current densities of ~41, ~83, and ~124 mA cm^{-2} when compared

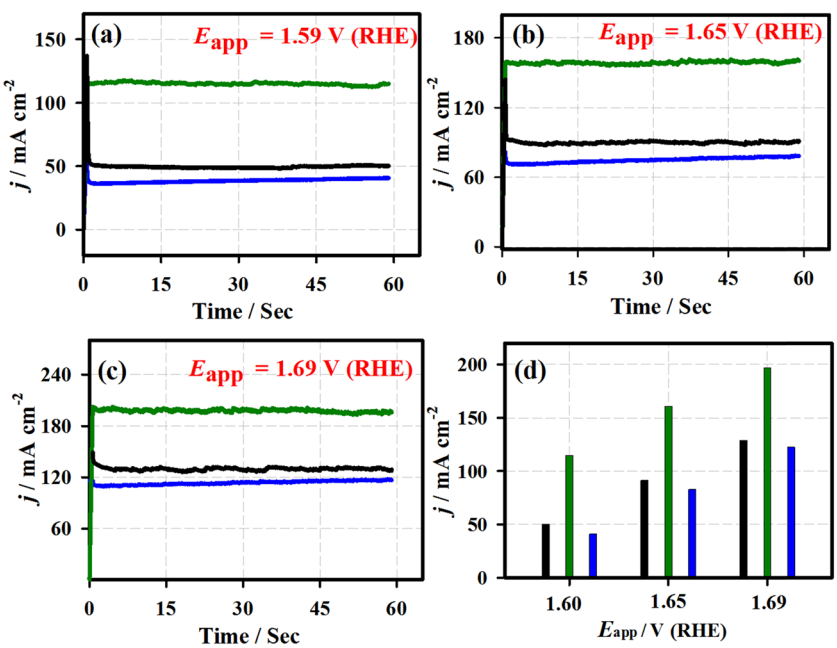

Fig. 5 Chronoamperometric response of the 3D-FeO NS|NF (black curve), FeCoO NC@3D-FeCoO NS|NF (green curve), 3D-CoO NS|NF (blue curve) and commercial RuO_2 (dark red curve) electrodes under the applied electrode potentials of 1.59 V (a), 1.65 V (b), and 1.69 V (c). The plot of measured current density against the different applied potentials of the developed electrodes (d).

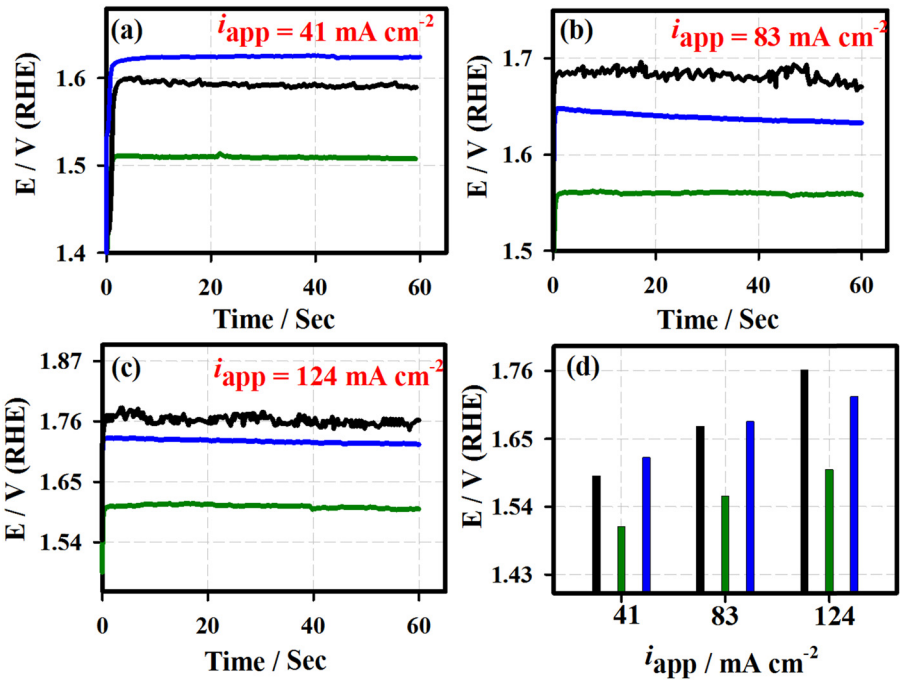

Fig. 6 Chronopotentiometric response of the 3D-FeO NS|NF (black curve), FeCoO NC@3D-FeCoO NS|NF (green curve), 3D-CoO NS|NF (blue curve) and commercial RuO_2 (dark red curve) electrodes under the applied current densities of ~40 mA cm^{-2} (a), ~80 mA cm^{-2} (b), and ~125 mA cm^{-2} (c). The plot of measured electrode potentials against the different applied current densities of the developed electrodes (d).

to other electrodes investigated in this study. The FeCoO NC@3D-FeCoO NS|NF electrode exhibited 1.50, 1.55, and 1.60 V at the applied current densities of ~41, ~83, and ~124 mA cm^{-2}, which is less positive in comparison to 3D-FeO NS|NF and 3D-CoO NS|NF electrodes, respectively.

Fig. 7 displays the Nyquist plots of the 3D-FeO NS|NF (a), FeCoO NC@3D-FeCoO NS|NF (b), 3D-CoO NS|NF (c) electrodes recorded at the various applied potentials of 1.60 V (blue curve), 1.65 V (red curve) and 1.69 V (green curve) in 1.0 M KOH. In Fig. 7, the EIS data (dotted curve) were fitted with the electronic equivalent circuit (solid curve). As depicted in Fig. 7, the FeCoO NC@3D-FeCoO NS|NF electrode exhibited the smallest polarization resistance (R_p) of ~2.1, ~1.1, and ~1.0 Ω at the applied potentials of 1.60 V, 1.65 V, and 1.69 V, respectively, when compared to the 3D-FeO NS|NF and 3D-CoO NS|NF electrodes, revealing the fast charge transfer process through the electrode/electrolyte interface. The electrochemical active surface area (ECASA) of the FeCoO NC@3D-FeCoO NS|NF electrode was calculated based on the double layer capacitance (C_{dl}). Fig. S6 (ESI†) depicts the CV curves of the FeCoO NC@3D-FeCoO NS|NF electrode recorded in 1.0 M KOH with different scan rates (from 10.0 to 125.0 mV s^{-1}). The C_{dl} of the FeCoO NC@3D-FeCoO NS|NF electrode was calculated to be ~5.53 mF cm^{-2}, revealing the high ECASA values (~ 138.2) and a large amount of accessible active sites (~8.82 × 10^{-7} moles). The attained outstanding OER performance of the FeCoO NC@3D-FeCoO NS|NF electrode was due to the unique bimetallic heterostructure, rich in oxygen deficient sites and active sites, high ECASA, low polarization resistance, rapid charge-transfer kinetics, facilitation of mass diffusion/transport of OH^- ions and improved electronic conductivity, and ease of H_2O adsorption onto nearby active sites. The Fe–Co co-electron deficiency centers can prime the Co-sites to be highly active towards OH^- adsorption, and Co doping aids in improving the charge-transfer kinetics, increases the active sites, affords an optimized electronic structure, and improves the intrinsic catalytic activity. Moreover, the intermediates such as M–OH and M–O can be formed generally nearby the catalytic OER. The bonding interactions of M–O within the intermediates (M–OH, MO and MOOH) are crucial in the heterogeneous OER.

The stability performance of the FeCoO NC@3D-FeCoO NS|NF electrode was primarily evaluated by chronopotentiometric (E–t) measurements for 100 h in 1 M KOH at an applied current density of ~10 mA cm^{-2} (Fig. S7, ESI†). As depicted in Fig. S7 (ESI†), in the E–t test, the electrode potential reached ~1.71 V from ~1.65 V after the 100 h continuous OER test under an alkaline electrolyte. This result revealed that the as-developed FeCoO NC@3D-FeCoO NS|NF electrode was not only OER active but also demonstrated durable electrocatalytic OER performance. It is understood that the surface of the FeCoO NC@3D-FeCoO NS may be reconstructed as amorphous $Fe(OH)_2$ or $Co(OH)_2$ rather than crystalline FeCoO materials.[67,68] Thus, the present FeCoO NC@3D-FeCoO NS based electrode materials as efficient OER electrocatalysts can aid in improving the hydrogen-producing efficiency. Moreover, to test the overall water splitting, a two-electrode cell was constructed by using FeCoO NC@3D-FeCoO NS‖Pt/C (red line) as both anode and cathode. Fig. 8 displays the chronoamperometric curves of the FeCoO NC@3D-FeCoO NS‖Pt/C (red line) and RuO_2‖Pt/C (black curve) couples for overall water splitting

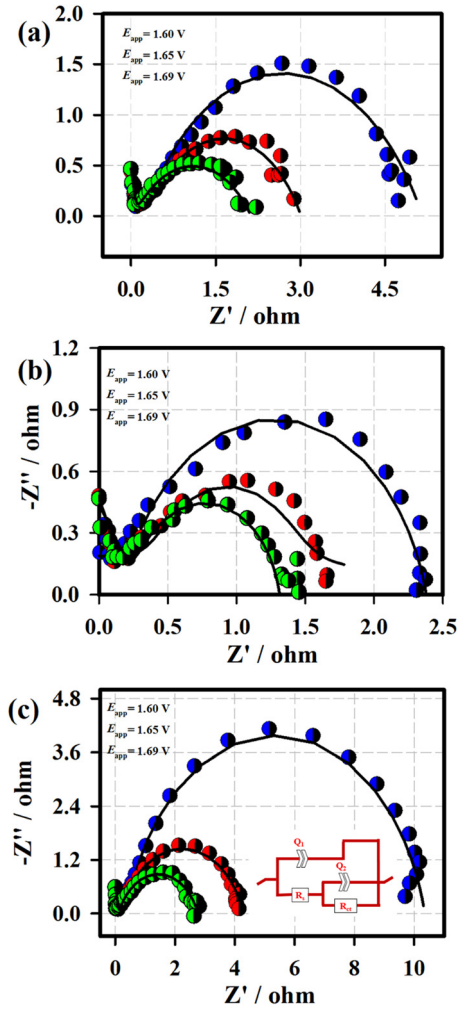

Fig. 7 Nyquist plots of the 3D-FeO NS|NF (a), FeCoO NC@3D-FeCoO NS|NF (b), and 3D-CoO NS|NF (c) electrodes recorded at the various applied potentials of 1.60 V (blue curve), 1.65 V (red curve) and 1.69 V (green curve) in 1.0 M KOH. Inset: Equivalent circuit for EIS fitting.

under an alkaline electrolyte at an applied potential of 1.99 V. As displayed in Fig. 8(a), the FeCoO NC@3D-FeCoO NS||Pt/C couple exhibited enormous OER activity with a current density of ~60 mA cm^{-2} after 5 h whereas the commercial RuO_2||Pt/C couple showed a current density of ~12 mA cm^{-2}. The developed FeCoO NC@3D-FeCoO NS||Pt/C electrode couple showed 5 times higher OER catalytic activity than the commercial RuO_2||Pt/C couple. Fig. 8(b) presents the LSV curves of the FeCoO NC@3D-FeCoO NS||Pt/C (red line) and RuO_2||Pt/C (black curve) couples recorded in 1.0 M KOH with a scan rate of 20 mV s^{-1}. As shown in Fig. 8(b), the FeCoO NC@3D-FeCoO NS|NF||Pt/C couple exhibited a less positive potential of ~1.82 V to attain a current density of ~50.0 mA cm^{-2}, which is ~150.0 mV smaller than that of the benchmark RuO_2||Pt/C couple in an alkaline electrolysis cell. Besides, the FeCoO NC@3D-FeCoO NS||Pt/C couple reached a higher current density of ~156.0 mA cm^{-2} at a potential of ~2.2 V in comparison to the commercial RuO_2||Pt/C couple, suggesting good practicability. The present nanoarchitecture of the hierarchical three-dimensional (3D) FeCoO NC@3D-FeCoO NS demonstrated the following features: (i) unique surface structures without any complicated procedures; (ii) *in situ* formation of nanoclusters on 3D nanosheets of FeCo oxides offering higher ECASA and more accessible active centers; (iii) high intrinsic catalytic OER activity of Fe–Co metal centers and their electronic structure; (iv) optimized bonding strength of metal centers with oxygen intermediates; (v) high dispersion of small-dimension of FeCo nanoclusters on 3D FeCo sheets facilitating the creation of oxyhydroxides; and (vi) the enormously increased number of active sites increasing the wettability of the nanostructures. These features aid in the enhancement of OER performance of the FeCoO NC@3D-FeCoO NS.

Conclusion

In summary, we demonstrated a facile, scalable, efficient and binder-free fabrication of earth-abundant bimetallic iron cobalt oxide nanoclusters embedded on 3D flower-like iron cobalt oxide nanosheet (FeCoO NC@3D-FeCoO NS) electrocatalysts with outstanding catalytic OER activity under an alkaline electrolyte. The FeCoO NC@3D-FeCoO NS|NF electrode exhibited a small overpotential (η) of ~0.22 V to drive an anodic current density of 10 mA cm^{-2} in 1.0 M KOH. The attained high catalytic activity of the fabricated FeCoO NC@3D-FeCoO NS|NF

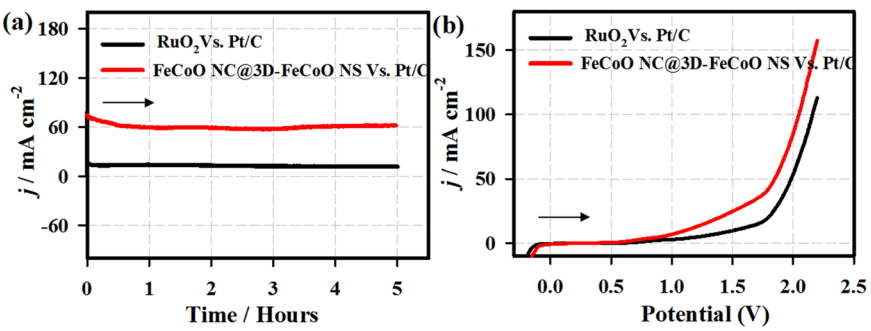

Fig. 8 Chronoamperometric curves of the FeCoO NC@3D-FeCoO NS||Pt/C (red line) and RuO_2||Pt/C (black curve) couples for overall water splitting (a). (b) LSV curves of the FeCoO NC@3D-FeCoO NS||Pt/C (red curve) and RuO_2||Pt/C (black line) couples recorded in 1.0 M KOH at a scan rate of 20 mV s^{-1} (b).

electrode arises not only from the large quantity of catalytically accessible active sites due to the smaller dimension of nanoclusters, but also from the improved activity of each catalytic site due to the interactions between Fe–Co metal centers and the rich oxygen deficient sites and active sites. The developed heterostructured FeCoO NC@3D-FeCoO NS also display an excellent durability without significant activity decay during the OER performance. In addition, the FeCoO NC@3D-FeCoO NS|NF‖Pt/C couple exhibited a less positive potential of ~1.82 V to attain a current density of 50 mA cm^{-2}, which is ~150.0 mV smaller than that of the benchmark RuO_2‖Pt/C couple in the alkaline electrolysis cell. It is therefore highly believed that the research findings of this study may provide insights into the design of novel non-precious electrocatalysts based on the nanocluster-based nanoarchitecture of hierarchical three-dimensional (3D) nanosheets towards the alkaline electrolyzer.

Conflicts of interest

There are no conflicts to declare.

Acknowledgements

This work was financially supported by the Central Power Research Institute (CPRI), Bangalore (Ref.: CPRI/R&D/TC/GDEC/2022). The authors also acknowledge the SRM Institute of Science and Technology (SRM IST) for providing all the research facilities, including SRM-SCIF for TEM measurements.

References

1 J. S. Kim, B. Kim, H. Kim and K. Kang, *Adv. Energy Mater.*, 2018, **8**, 1702774.
2 K. Zhu, X. Zhu and W. Yang, *Angew. Chem., Int. Ed.*, 2019, **58**, 1252–1265.
3 K. Wang, J. Huang, H. Chen, Y. Wang and S. Song, *Chem. Commun.*, 2020, **56**, 12109–12121.
4 P.-P. Liu, Y.-Q. Zheng, H.-L. Zhu and T.-T. Li, *ACS Appl. Nano Mater.*, 2019, **2**, 744–749.
5 H.-F. Wang, L. Chen, H. Pang, S. Kaskel and Q. Xu, *Chem. Soc. Rev.*, 2020, **49**, 1414–1448.
6 M. Ghaemmaghami, Y. Yamini, E. Saievar-Iranizad and A. Bayat, *Sustainable Energy Fuels*, 2020, **4**, 1150–1156.
7 Z. Wu, H. Wu, T. Niu, S. Wang, G. Fu, W. Jin and T. Ma, *ACS Sustainable Chem. Eng.*, 2020, **8**, 9226–9234.
8 T. Reier, M. Oezaslan and P. Strasser, *ACS Catal.*, 2012, **2**, 1765–1772.
9 S. Anantharaj, P. N. Reddy and S. Kundu, *Inorg. Chem.*, 2017, **56**, 1742–1756.
10 M. Hafezi Kahnamouei and S. Shahrokhian, *ACS Appl. Mater. Interfaces*, 2020, **12**, 16250–16263.
11 J. Huang and M. Eikerling, *Curr. Opin. Electrochem.*, 2019, **13**, 157–165.
12 R. Elakkiya and G. Maduraiveeran, *Langmuir*, 2020, **36**, 4728–4736.
13 C. Zhu, S. Fu, D. Du and Y. Lin, *Chem. – Eur. J.*, 2016, **22**, 4000–4007.
14 M. Wang, K. Cao, Z. Tian and P. Sheng, *Appl. Surf. Sci.*, 2019, **493**, 351–358.
15 G. Maduraiveeran, M. Sasidharan and W. Jin, *Prog. Mater. Sci.*, 2019, **106**, 100574.
16 P. Ramakrishnan, K. B. Lee and J. I. Sohn, *Appl. Surf. Sci.*, 2021, **566**, 150653.
17 B. Sidhureddy, J. S. Dondapati and A. Chen, *Chem. Commun.*, 2019, **55**, 3626–3629.
18 R. Zhao, J. Chen, Z. Chen, X. Jiang, G. Fu, Y. Tang, W. Jin, J.-M. Lee and S. Huang, *ACS Appl. Energy Mater.*, 2020, **3**, 4539–4548.
19 P. Zhai, Y. Zhang, Y. Wu, J. Gao, B. Zhang, S. Cao, Y. Zhang, Z. Li, L. Sun and J. Hou, *Nat. Commun.*, 2020, **11**, 5462.
20 W. Wang, M. Xu, X. Xu, W. Zhou and Z. Shao, *Angew. Chem., Int. Ed.*, 2020, **59**, 136–152.
21 Z. Yan, H. Sun, X. Chen, H. Liu, Y. Zhao, H. Li, W. Xie, F. Cheng and J. Chen, *Nat. Commun.*, 2018, **9**, 2373.
22 G. Ou, F. Wu, K. Huang, N. Hussain, D. Zu, H. Wei, B. Ge, H. Yao, L. Liu, H. Li, Y. Shi and H. Wu, *ACS Appl. Mater. Interfaces*, 2019, **11**, 3978–3983.
23 H. Sun, Z. Yan, F. Liu, W. Xu, F. Cheng and J. Chen, *Adv. Mater.*, 2020, **32**, 1806326.
24 S. Ren, X. Duan, F. Ge, M. Zhang and H. Zheng, *J. Power Sources*, 2020, **480**, 228866.
25 M. Cai, W. Liu, X. Luo, C. Chen, R. Pan, H. Zhang and M. Zhong, *ACS Appl. Mater. Interfaces*, 2020, **12**, 13971–13981.
26 H. Qin, Y. He, P. Xu, D. Huang, Z. Wang, H. Wang, Z. Wang, Y. Zhao, Q. Tian and C. Wang, *Adv. Colloid Interface Sci.*, 2021, **294**, 102486.
27 S. Zhu, J. Lei, Y. Qin, L. Zhang and L. Lu, *RSC Adv.*, 2019, **9**, 13269–13274.
28 T. Kesavan, S. Boopathi, M. Kundu, G. Maduraiveeran and M. Sasidharan, *Electrochim. Acta*, 2018, **283**, 1668–1678.
29 W. Wang, L. Kuai, W. Cao, M. Huttula, S. Ollikkala, T. Ahopelto, A.-P. Honkanen, S. Huotari, M. Yu and B. Geng, *Angew. Chem., Int. Ed.*, 2017, **56**, 14977–14981.
30 Y. Huang, W. Yang, Y. Yu and S. Hao, *J. Electroanal. Chem.*, 2019, **840**, 409–414.
31 M. Li, Y. Xiong, X. Liu, X. Bo, Y. Zhang, C. Han and L. Guo, *Nanoscale*, 2015, **7**, 8920–8930.
32 H. S. Jadhav, A. Roy, G. M. Thorat and J. G. Seo, *Inorg. Chem. Front.*, 2018, **5**, 1115–1120.
33 M. Lu, L. Wang, B. Jiang and J. Zheng, *J. Electrochem. Soc.*, 2019, **166**, D69–D76.
34 K. L. Yan, X. Shang, Z. Z. Liu, B. Dong, S. S. Lu, J. Q. Chi, W. K. Gao, Y. M. Chai and C. G. Liu, *Int. J. Hydrogen Energy*, 2017, **42**, 24150–24158.
35 D. Guo, H. Kang, P. Wei, Y. Yang, Z. Hao, Q. Zhang and L. Liu, *CrystEngComm*, 2020, **22**, 4317–4323.
36 H. A. Bandal, A. R. Jadhav, A. H. Tamboli and H. Kim, *Electrochim. Acta*, 2017, **249**, 253–262.
37 K.-H. Kim and Y.-H. Choi, *Electrochim. Acta*, 2021, **395**, 139195.

38 C. Yuan, J. Li, L. Hou, X. Zhang, L. Shen and X. W. D. Lou, *Adv. Funct. Mater.*, 2012, **22**, 4592–4597.
39 R. Li, Y. Li, P. Yang, D. Wang, H. Xu, B. Wang, F. Meng, J. Zhang and M. An, *J. Energy Chem.*, 2021, **57**, 547–566.
40 S. Yoon, J. Kim, J.-H. Lim and B. Yoo, *J. Electrochem. Soc.*, 2018, **165**, H271–H276.
41 X. Li, Y. Wang, J. Wang, Y. Da, J. Zhang, L. Li, C. Zhong, Y. Deng, X. Han and W. Hu, *Adv. Mater.*, 2020, **32**, 2003414.
42 R. Chaabani, A. Lamouchi, B. Mari and R. Chtourou, *Mater. Res. Express*, 2019, **6**, 115902.
43 Z. W. Seh, J. Kibsgaard, C. F. Dickens, I. Chorkendorff, J. K. Nørskov and T. F. Jaramillo, *Science*, 2017, **355**(6321), 1–12.
44 J. Chen, G. Zhao, Y. Chen, K. Rui, H. Mao, S. X. Dou and W. Sun, *Chem. – Eur. J.*, 2019, **25**, 280–284.
45 Y. Qiu, L. Xin and W. Li, *Langmuir*, 2014, **30**, 7893–7901.
46 T. Li, Y. Lv, J. Su, Y. Wang, Q. Yang, Y. Zhang, J. Zhou, L. Xu, D. Sun and Y. Tang, *Adv. Sci.*, 2017, **4**, 1700226.
47 G. Ou, F. Wu, K. Huang, N. Hussain, D. Zu, H. Wei, B. Ge, H. Yao, L. Liu, H. Li, Y. Shi and H. Wu, *ACS Appl. Mater. Interfaces*, 2019, **11**, 3978–3983.
48 X. Gu, D. Yang, Z. Liu, S. Wang and L. Feng, *Electrochim. Acta*, 2020, **353**, 136516.
49 A. El Bachiri, L. Soussi, O. Karzazi, A. Louardi, A. Rmili, H. Erguig and B. El Idrissi, *Spectrosc. Lett.*, 2019, **52**, 66–73.
50 T. Wang, M. Liu and H. Ma, *Nanomaterials*, 2017, **7**, 140.
51 M. A. Sayeed and A. P. O'Mullane, *ChemPhysChem*, 2019, **20**, 3112–3119.
52 L. Zhuang, L. Ge, Y. Yang, M. Li, Y. Jia, X. Yao and Z. Zhu, *Adv. Mater.*, 2017, **29**, 1606793.
53 P. Wang and B. Wang, *ChemSusChem*, 2020, **13**, 4795–4811.
54 K. Ao, D. Li, Y. Yao, P. Lv, Y. Cai and Q. Wei, *Electrochim. Acta*, 2018, **264**, 157–165.
55 D. Zhong, L. Liu, D. Li, C. Wei, Q. Wang, G. Hao, Q. Zhao and J. Li, *J. Mater. Chem. A*, 2017, **5**, 18627–18633.
56 Q. Qian, J. Zhang, J. Li, Y. Li, X. Jin, Y. Zhu, Y. Liu, Z. Li, A. El-Harairy, C. Xiao, G. Zhang and Y. Xie, *Angew. Chem., Int. Ed.*, 2021, **60**, 5984–5993.
57 L. Zhuang, Y. Jia, H. Liu, Z. Li, M. Li, L. Zhang, X. Wang, D. Yang, Z. Zhu and X. Yao, *Angew. Chem., Int. Ed.*, 2020, **59**, 14664–14670.
58 D. Rakov, C. Sun, Z. Lu, S. Li and P. Xu, *Adv. Energy Sustainable Res.*, 2021, **2**, 2100071.
59 J. Han, G. Chen, X. Liu, N. Zhang, S. Liang, R. Ma and G. Qiu, *Chem. Commun.*, 2019, **55**, 9212–9215.
60 S. Wu, Y. Qi, Q. Wang, X. Wang, X. Zhao and E. Yang, *ChemElectroChem*, 2020, **7**, 684–690.
61 B. B. Gicha, L. T. Tufa, Y. Choi and J. Lee, *ACS Appl. Energy Mater.*, 2021, **4**, 6833–6841.
62 Y. Li, P. Hasin and Y. Wu, *Adv. Mater.*, 2010, **22**, 1926–1929.
63 Y. Zhou, J. Hu, D. Li and Q. Gao, *Chem. Commun.*, 2021, **57**, 7653–7656.
64 L. Bai, C.-S. Hsu, D. T. L. Alexander, H. M. Chen and X. Hu, *J. Am. Chem. Soc.*, 2019, **141**, 14190–14199.
65 Q. Chen, Y. Fu, J. Jin, W. Zang, X. Liu, X. Zhang, W. Huang, Z. Kou, J. Wang, L. Zhou and L. Mai, *J. Energy Chem.*, 2021, **55**, 10–16.
66 T. I. Singh, G. Rajeshkhanna, U. N. Pan, T. Kshetri, H. Lin, N. H. Kim and J. H. Lee, *Small*, 2021, **17**, 2101312.
67 J.-H. Park, S. Woo, J. Lee, H. Y. Jung, J. C. Ro, C. Park, B. Lim and S.-J. Suh, *Int. J. Hydrogen Energy*, 2021, **46**, 15398–15409.
68 M. A. Sayeed and A. P. O'Mullane, *ChemPhysChem*, 2019, **20**, 3112–3119.